Nano Research 2018, 11(4): 2104–2115
https://doi.org/10.1007/s12274-017-1828-4
Research Article

ISSN 1998-0124
CN 11-5974/O4

Temperature modulation of concentration quenching in lanthanide-doped nanoparticles for enhanced upconversion luminescence

Luoyuan Li[1,§], Ningjiu Zhao[1,2,§], Limin Fu[1] (✉), Jing Zhou[3], Xicheng Ai[1], and Jianping Zhang[1]

[1] *Department of Chemistry, Renmin University of China, Beijing 100872, China*
[2] *State Key Laboratory of Molecular Reaction Dynamics, Dalian Institute of Chemical Physics, Chinese Academy of Sciences, Dalian 116023, China*
[3] *Department of Chemistry, Capital Normal University, Beijing 100048, China*
[§] *Luoyuan Li and Ningjiu Zhao contributed equally to this work.*

Received: 14 June 2017
Revised: 10 August 2017
Accepted: 29 August 2017

KEYWORDS

upconversion luminescence, lanthanide-doped nanoparticle, temperature modulation, concentration quenching, energy transfer

ABSTRACT

The doping concentration of lanthanide ions is important for manipulating the luminescence properties of upconversion nanoparticles (UCNPs). However, the serious concentration quenching in highly doped UCNPs remains a vital restriction for further enhanced upconversion luminescence (UCL). Herein, we examined the effect of temperature on the concentration quenching of rare-earth UCNPs, an issue that has been overlooked, and we show that it is significant for biomedical or optical applications of UCNPs. In this work, we prepared a series of UCNPs by doping Er^{3+} luminescent centers at different concentrations in a $NaLuF_4$:Yb^{3+} matrix. At room temperature (298 K), steady-state photoluminescence (PL) spectroscopy showed substantial concentration quenching of the Er^{3+} emission with increasing doping concentrations. However, the concentration quenching effect was no longer effective at lower temperatures. Kinetic curves obtained from time-resolved PL spectroscopy further showed that the concentration quenching dynamics were vitally altered in the cryogenic temperature region, i.e., below 160 K. Our work on the temperature-switchable concentration quenching mechanism may shed light on improving UCL properties, promoting their practical applications.

1 Introduction

Since the concept of upconversion luminescence (UCL) was officially put forward in the 1960s [1–3], structural optimization of lanthanide-doped nanomaterials has drawn a great deal of attention for potential applications in biosensors, luminescent probes, and display devices [4–10]. Lanthanide-doped nanomaterials exhibit unique

---

Address correspondence to lmfu@ruc.edu.cn

luminescence properties, such as a large anti-Stokes shift of several hundred nanometers, sharp emission line, long lifetime, and superior photo-stability, under a near-infrared laser [11–18]. In lanthanide-doped nanomaterials, the upconversion process is generally separated into excitation energy absorption, various energy migration, energy transfer upconversion (ETU), and radiative transition, while the process occurs within different central ions [1, 19, 20]. However, the low quantum efficiency and luminescence intensity of rare earth (RE) nanomaterials produce certain restrictions on promoting their practical applications. The most vital restriction is that the doping concentration of luminescent central ions (e.g., Er^{3+}, Tm^{3+}) is always set below 5 mol.%. When high doping concentrations were maintained, lanthanide-doped nanomaterials showed significantly weaker luminescence intensities because of so-called "concentration quenching" [21, 22], which was caused by various degrees of non-radiative relaxation, including cross relaxation (CR) [23, 24] and cascade energy transfer to intracellular defects and surface defects.

Recently, numerous efforts have been attempted to overcome the concentration limitation of upconversion nanomaterials to obtain enhanced UCL properties [20, 25–30]. These improvements mainly include modulating a high laser power density, designing spatial separation, optimizing energy clustering at the sublattice level, and using organic dye sensitization. Despite the slight improvement of the restrictions using these methods, the concentration quenching was not completely clarified from the mechanism. Essentially, the cascade energy transfer to surface defects was considered as the main origin of concentration quenching from environmentally sensitive surface atoms in nanomaterials. However, most researchers have not focused on the temperature dependence of concentration quenching in the past decades [1, 31, 32]. Therefore, a systematic study should be undertaken with respect to the temperature effect on concentration quenching to further understand its mechanism in upconversion nanomaterials.

In this work, hexagonal phase (β)-$NaLuF_4$:20%Yb^{3+} upconversion nanoparticles (UCNPs) with different Er^{3+} doping concentrations (2%, 5%, 10%, and 20%, molar concentration) were selected to study the effect of temperature modulation on the concentration quenching mechanism. We also examined the steady-state photoluminescence (PL) and nanosecond time-resolved PL spectra as the temperature changed from 300 to 77 K. These UCNPs showed obvious temperature dependences and significant concentration quenching at room temperature in the PL spectra. However, the concentration quenching almost completely disappeared at cryogenic temperatures. We further explored the temperature effect through time-resolved PL spectra, which indicated that the temperature is vital to the concentration quenching process in nanomaterials at high doping concentrations. Our results highlight the effect of temperature on the concentration quenching mechanism to solve the doping concentration limitation and promote practical applications of RE nanomaterials.

2 Results and discussion

In this work, $NaLuF_4$:20%Yb^{3+} nanoparticles with different Er^{3+} doping concentrations (molar concentrations of 2%, 5%, 10%, and 20% for sample 1, sample 2, sample 3, and sample 4, respectively; Scheme 1(a)) were obtained using a conventional solvothermal method [33–38]. The morphology and size were characterized by transmission electron microscopy (TEM), and the four samples show uniform spherical morphologies (Fig. 1(a)). The high-resolution TEM image (Fig. 1(b)) shows that the lattice fringes of the four samples are in good agreement with the planes (222 and 100) of the hexagonal phase (β-phase) of $NaLuF_4$ (JCPDS card No. 27-0726). However, β-phase nanomaterials show stronger UCL properties than α-phase nanomaterials [39–42]. The dynamic light scattering (DLS) data (Fig. 1(c)) show narrow particle size distributions (sample 1: 42 ± 2 nm, sample 2: 39 ± 1.5 nm, sample 3: 37 ± 2 nm, sample 4: 35 ± 3 nm). The X-ray diffraction (XRD) measurements (Fig. 2) also show that the crystal phases of the four samples correspond to the standard data of the β-phase of $NaLuF_4$ (JCPDS card No. 27-0726) without any interfering peaks [43–47].

The UCL properties of the four samples were investigated by temperature-dependent steady-state PL spectroscopy under a 980-nm continuous-wave

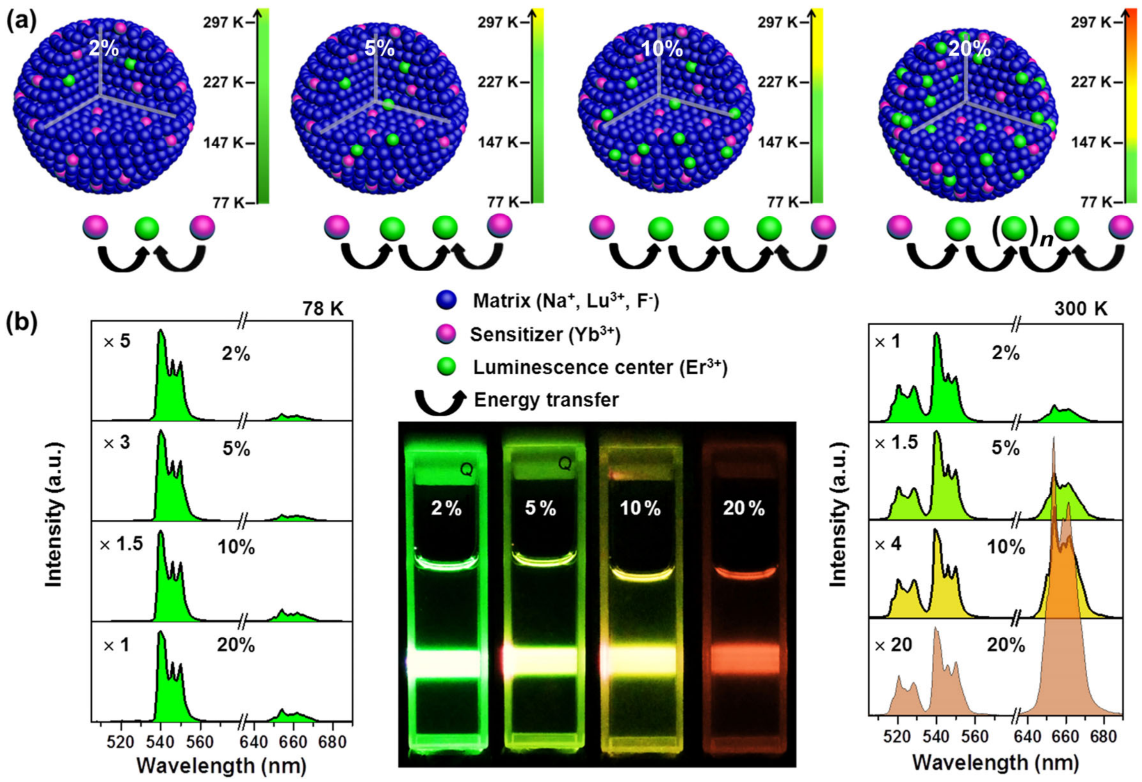

Scheme 1 (a) Schematic images of four nanoparticles with different doping concentrations of Er^{3+} ions (2%, 5%, 10%, and 20%) and different energy transfer modes. (b) Luminescence photos (300 K) and luminescence spectra (78 and 300 K) of the four samples.

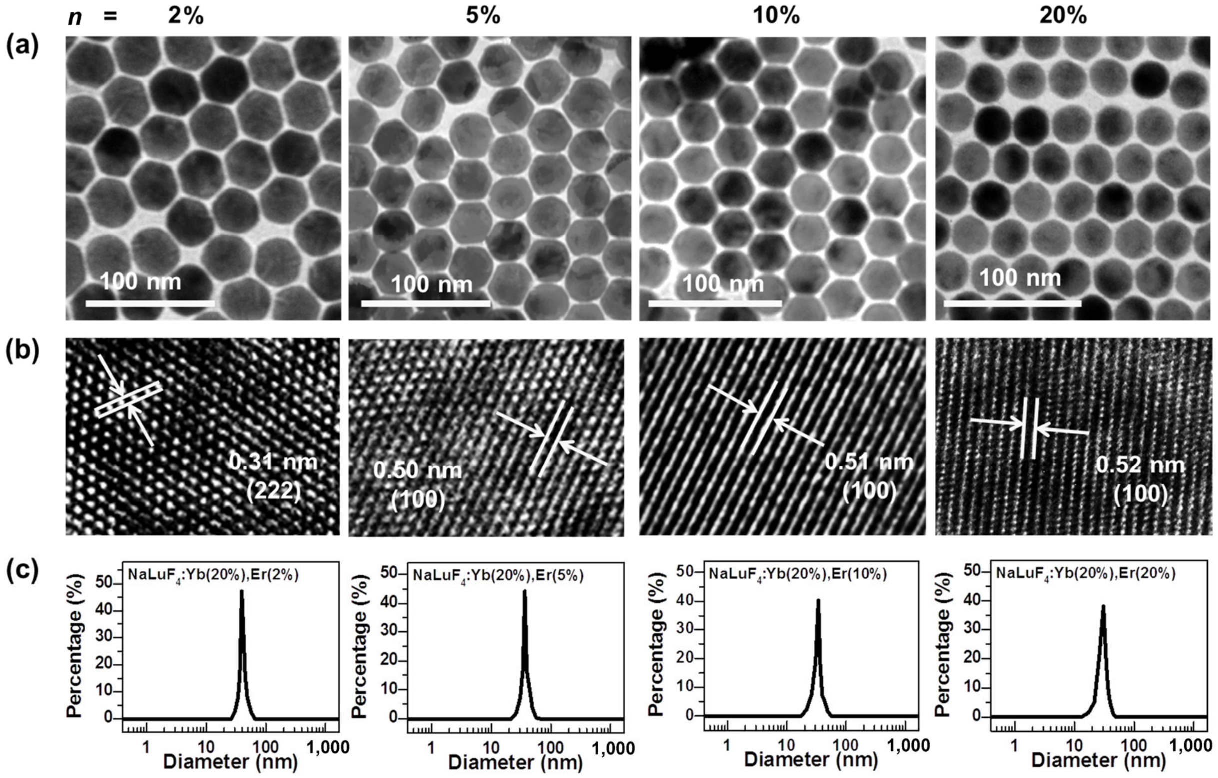

Figure 1 Characterization of $NaLuF_4$:20%Yb^{3+}, nEr^{3+} nanoparticles, n = 2%, 5%, 10%, or 20%. (a) TEM images, (b) high-resolution TEM images, and (c) DLS data.

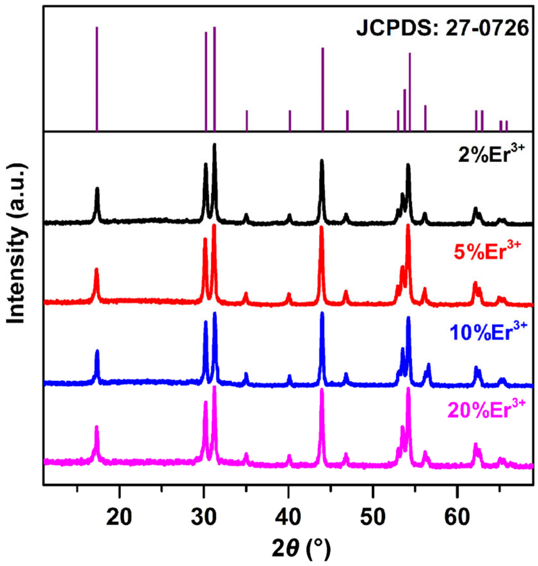

Figure 2 XRD data for the NaLuF$_4$:20%Yb^{3+}, nEr^{3+} nanoparticles (n = 2%, 5%, 10%, and 20%).

(CW) laser excitation. Scheme 1(b) shows that the UCL color changes from green to orange as the Er^{3+} doping concentration increases from 2% to 20%. The spectra of the four samples show systematic changes as the temperature decreases from 310 to 77 K (Fig. 3). The emission peaks can be attributed to $^2H_{9/2} \rightarrow {}^4I_{15/2}$ (410 nm), $^2H_{11/2} \rightarrow {}^4I_{15/2}$ (521 nm), $^4S_{3/2} \rightarrow {}^4I_{15/2}$ (542 nm), and $^4F_{9/2} \rightarrow {}^4I_{15/2}$ (655 nm) transitions of Er^{3+} [48–54]. At 300 K, samples with higher doping concentrations show weaker UCL intensities and higher red/green ratios ($R_{r/g}$) from sample 1 to sample 4, showing the significantly enhanced concentration quenching. The two green emissions (521 and 542 nm) of Er^{3+} could be discussed together because their populations are mainly controlled by thermal activation (Fig. S4 in the Electronic Supplementary Material (ESM)). In Fig. 4, the UCL intensities of the red emission (UCL centered

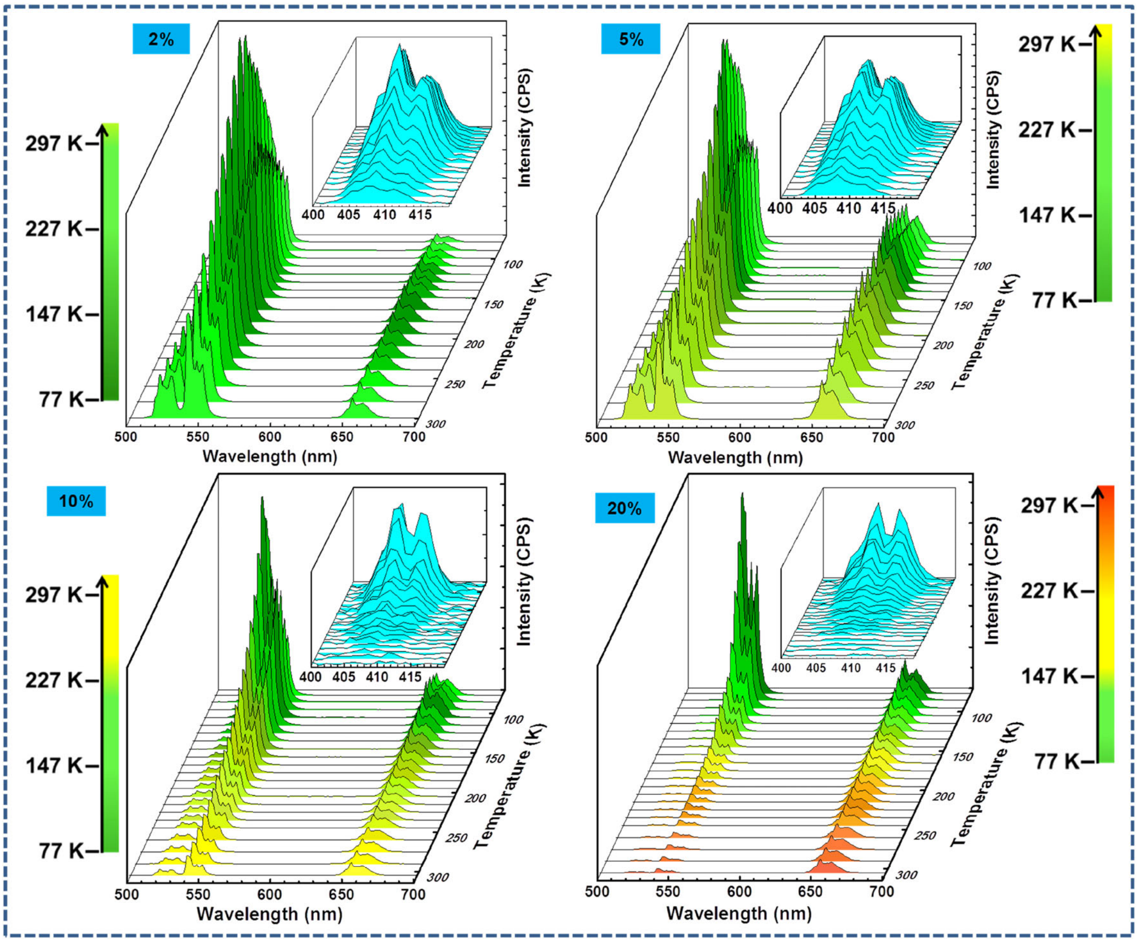

Figure 3 Steady-state PL spectra at different temperatures (77–310 K) of NaLuF$_4$:20%Yb^{3+}, nEr^{3+} nanoparticles under a 980-nm laser irradiation (0.55 W), n = 2%, 5%, 10%, and 20%.

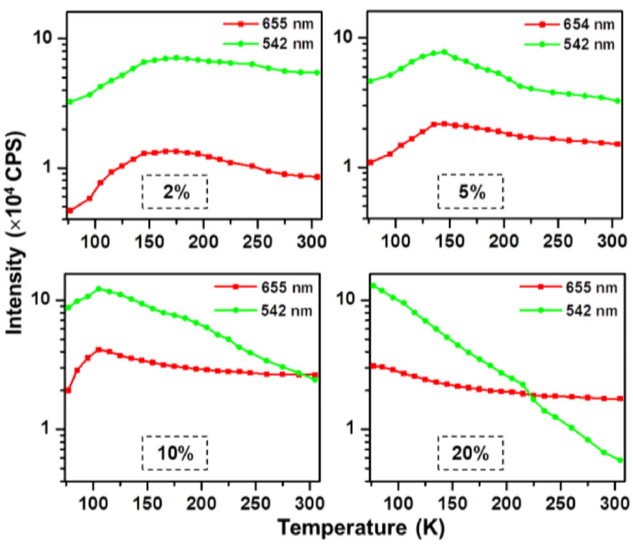

Figure 4 Scatter diagrams of steady-state PL intensities at different temperatures for the 542- and 655-nm emissions of $NaLuF_4$:20%Yb^{3+}, $n$$Er^{3+}$ nanoparticles under 980-nm laser irradiation (0.55 W), n = 2%, 5%, 10%, and 20%.

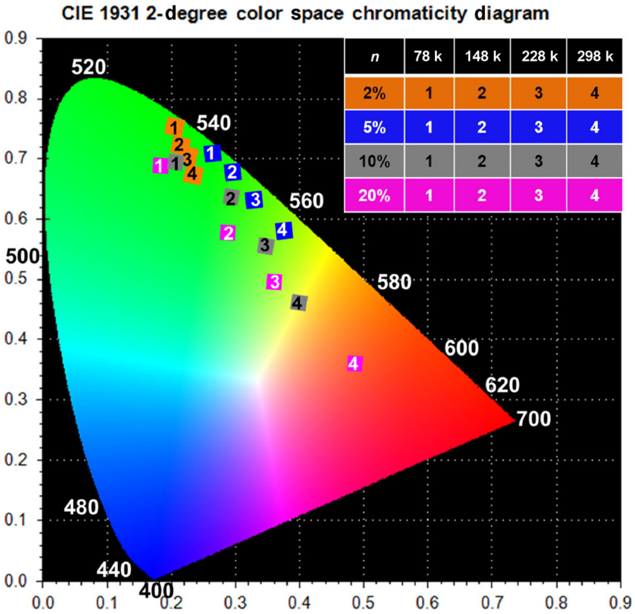

Figure 5 Luminescence color space chromaticity diagram of $NaLuF_4$:20%Yb^{3+}, $n$$Er^{3+}$ nanoparticles at different temperatures (n = 2%, 5%, 10%, and 20%).

at 655 nm) and green emission (UCL centered at 542 nm) significantly increase with cooling from 300 to 160 K (Fig. S1 in the ESM). The ratios ($R_{r/g}$) between the red emission and green emission intensities of Er^{3+} vs. the temperature (78–300 K) in the four samples are depicted. The green emission increases more significantly than the red emission as the temperature decreases from 300 to 160 K, resulting in the green color of the nanoparticles. The color space chromaticity diagram (Fig. 5) corresponding to the steady-state PL spectra at 78, 140, 220, and 300 K is depicted to more easily observe the changes in the color of the luminescence.

As shown in Fig. 4, the UCL intensities of the green and red emissions in sample 1 increase upon cooling and show a maximum intensity point (MIP) at ~ 160 K and then decreased with cooling to 77 K. The other three samples show similar behaviors, but the MIPs occur at different temperatures. For sample 2 and sample 3, the MIPs occur at 140 and 100 K, respectively; for sample 4, the MIP cannot be observed within the temperature range of our experiment. The UCL intensities increasing with cooling to the MIP temperature (T_{MIP}) can be easily explained by the restraint of the excitation energy dissipation processes. The different temperature-dependent behavior of the samples with higher Er^{3+} doping concentrations and the decreasing UCL intensities in the cryogenic temperature region show that the microscopic processes that control the UCL properties of the UCNPs are not in a straight path.

In the cryogenic temperature region (from 77 K to T_{MIP}), the four samples show similar maximum UCL intensities, indicating that the concentration quenching is switched off. Many researchers have shown that the populations of Er^{3+} at higher energy levels require multi-step cascading ETUs and CR processes among the ions [49, 55]. Because of the particularity of the energy levels in lanthanide ions, there are many energy mismatches in the ETU and CR processes, which always require thermal activation. The population of an emitting level through more complicated energy transfer processes always places more demands on the thermal activation. For samples 1, 2, and 3 at cryogenic temperatures, the UCL enhancement with increasing temperature could be attributed to the increased probabilities of the ETU processes by thermal activation. The ETU processes result from interactions within different energy levels of Yb^{3+} and Er^{3+} under thermal control. In the upconversion nanocrystals, many excitation energy donor–acceptor (D–A) channels may exist. Only partial D–A channels are efficient and can easily achieve balance through energy transfer, and the ETU process in the Yb^{3+}-Er^{3+} system proceeds through this channel. Other D–A channels of mismatched energy levels can hardly achieve a balance without the help of thermal activation, so that the CR process can be significantly enhanced at higher temperatures. Therefore, the two kinds of channels have different dependences on the temperature. Overall, the energy transfer channel is the ETU process, which is less dependent on temperature, while the CR process is highly dependent on the temperature. Therefore, the population of higher emitting levels shows various temperature effects in UCNPs with different Er^{3+} doping concentrations, i.e., the samples with higher Er^{3+} doping concentrations produce lower T_{MIP} values, which show more obvious concentration dependences.

As the temperature further increases to 300 K, the UCL intensities of the four samples decrease to different degrees (Fig. 4). The amounts of change are quite different, i.e., higher Er^{3+} doping concentrations (sample 3 and sample 4) more severely decrease the UCL intensities of the 542-nm emission. These phenomena could not be merely attributed to thermally dependent non-radiative transitions. In the samples with higher Er^{3+} doping concentrations, higher emitting level deactivations result from thermally activated ion interactions, which are concentration quenching. The UCL intensities of the 542-nm emission decrease more significantly than the UCL intensities of the 655-nm emission. This phenomenon could be attributed to concentration quenching of the $^4S_{3/2}$ level (542 nm), which partially populates the $^4F_{9/2}$ energy level (655 nm), i.e., the energy from the Er^{3+} ion of the $^4S_{3/2}$ level is transferred to a nearby Er^{3+} ion at the $^4I_{13/2}$ energy level, and the Er^{3+} ion is generated from the 655-nm emission ($^4S_{3/2} + {}^4I_{13/2} \rightarrow {}^4I_{11/2} + {}^4F_{9/2}$) [19].

Furthermore, the variation in the green emission intensity is more obvious than that of the red emission intensity, leading to an enhanced $R_{r/g}$ value at 300 K as the Er^{3+} doping concentration increases (Fig. S2 in the ESM). The subtle changes of the red and green emissions in the four samples as the temperature increases indicates that more complicated microscopic interactions exist in the UCL processes. For samples 1–3, the enhancement slopes of the 542-nm emission are lower than that of the 655-nm emission as the temperature increases from 77 K to T_{MIP} (Fig. 4) because of the more complicated population process at the 655-nm emitting level. It can also be explained by the more complex population process (Fig. 6(a)) of the red emission (three successive ETUs and a one-step CR process) than green emission (two successive ETU processes). As the temperature increases from T_{MIP} to 300 K, the slopes of the 655-nm emissions decrease

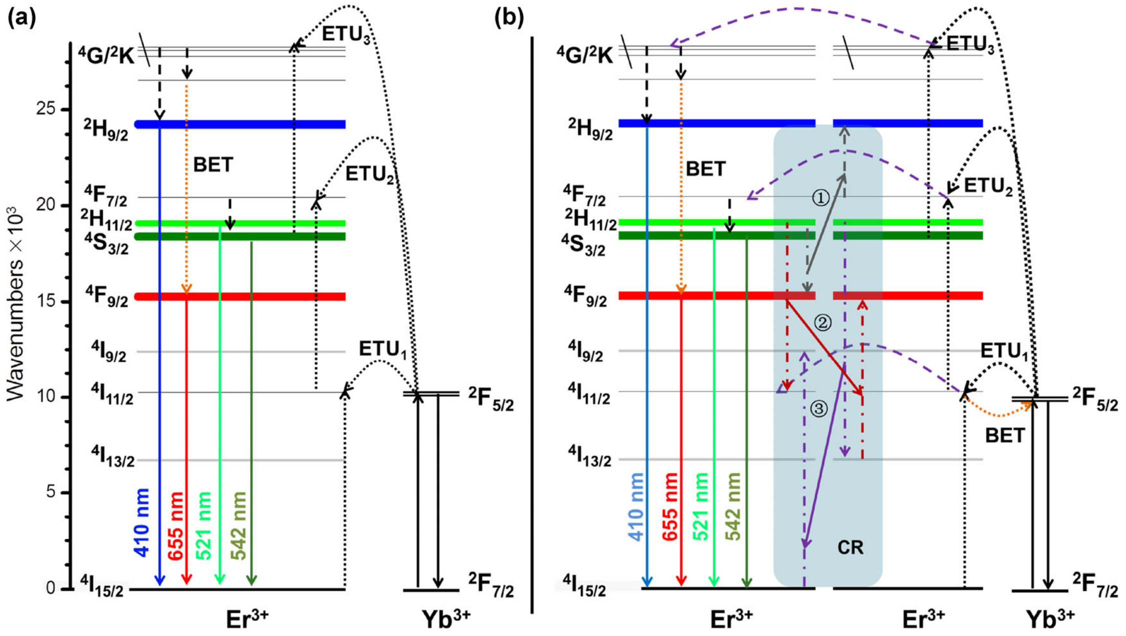

Figure 6 Energy transfer between the sensitizer ions (Yb^{3+}) and luminescent central ions (Er^{3+}) in the nanoparticles at (a) low temperatures and (b) high temperatures. Note: ETU = energy transfer upconversion, CR = cross relaxation, BET = back transfer.

significantly less than that of the green emission, especially for samples 2–4 (UCNPs with higher Er^{3+} doping concentrations). As mentioned above, the UCL decrease is mainly caused by thermally dependent non-radiative transitions and the excited state deactivation results from interactions between ions (corresponding to concentration quenching). If sample 1 has no concentration quenching, the UCL decrease of the red and green emissions could be attributed to the different temperature parameters of the thermally dependent non-radiative transitions (i.e., the former reason). For samples 2–4, the decrease of the green emission shows that the temperature dependence is enhanced as the Er^{3+} doping concentration increases, mainly because of the concentration quenching (i.e., the latter reason).

To further investigate the dependence of the ETU population and UCL process on temperature, the kinetic curves of the $^4S_{3/2}$ (542 nm) and $^4F_{9/2}$ (655 nm) levels were explored for the four samples (Fig. 7). In the four samples, the effect of temperature on the kinetics is enhanced with increasing Er^{3+} doping concentrations. These kinetic curves were fitted with a bi-exponential equation, as follows

$$I_t = A_1 \exp(-t/\tau_{\text{rise}}) + A_2 \exp(-t/\tau_{\text{decay}}) \qquad (1)$$

where τ_{rise} and τ_{decay} represent the rising and the decay time constants, respectively, which describe the time scales of the population and depopulation, respectively, for the corresponding energy levels. From the dynamic results at different temperatures for each of the four samples, the decay phase of the process could greatly influence the increasing phase, and the apparent parameters of τ_{rise} do not show useful information. As the Er^{3+} doping concentration increases, τ_{decay} decreases significantly near room temperature. For example, at 300 K, the τ_{decay} values for samples 1, 2, 3, and 4 are 221.3, 164.1, 68.7, and 10.8 μs, respectively, at 542 nm and 386.4, 310.8, 173.4, and 71.7 μs, respectively, at 655 nm. This indicates obvious concentration quenching near room temperature and significantly inhibited concentration quenching at low temperatures. In the cryogenic temperature region, the τ_{decay} parameters at 542 and 655 nm slightly increase with increasing Er^{3+} doping concentrations from 2% to 20%, implying that the population of green emission levels in a single particle can be enhanced at higher Er^{3+} doping concentrations after the concentration quenching is restrained.

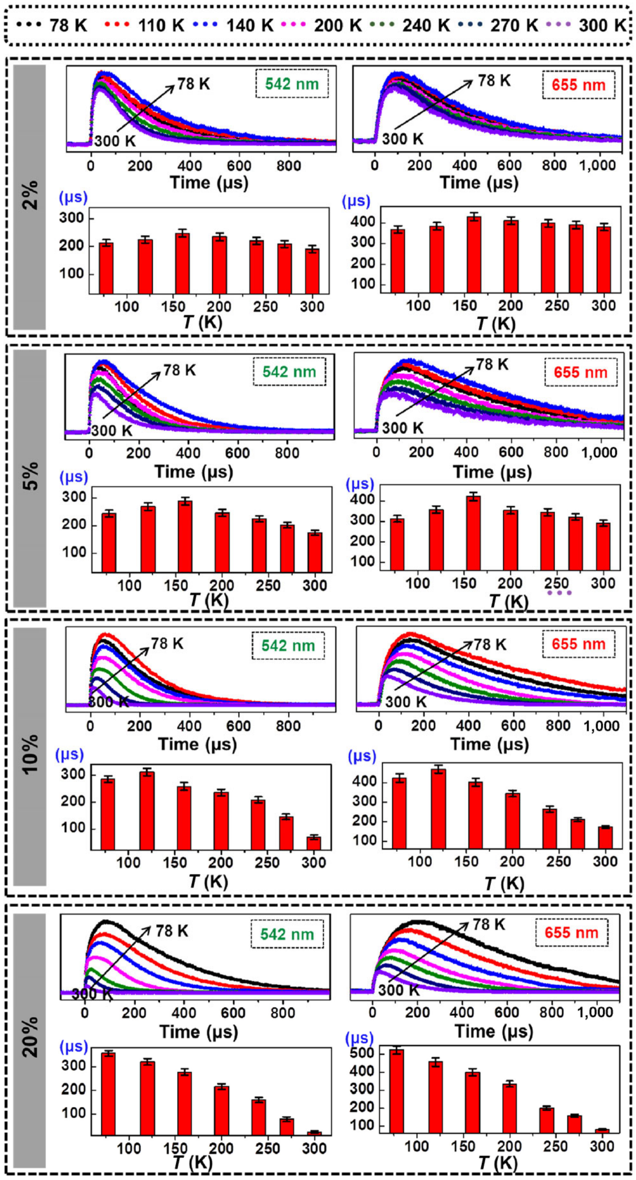

Figure 7 Dependence of the kinetic curves and fitting lifetimes of the $^4S_{3/2}$ (542 nm) and $^4F_{9/2}$ (655 nm) levels on the temperature (78–300 K) of NaLuF$_4$:20%Yb^{3+}, nEr^{3+} nanoparticles (n = 2%, 5%, 10%, and 20%).

With changing temperature, the luminescence lifetime variations at 542 and 655 nm for sample 1 (see the first panel of Fig. 7 and Figs. S2 and S3 in the ESM) are consistent with the temperature dependence of the steady-state PL intensities (see Fig. 4). This indicates that the temperature effect on the UCL intensity could be directly explained by the thermally activated non-radiative transitions. In samples 2–4, the transient intensities and τ_{decay} values of the luminescence kinetics at 542 nm strongly decrease as the temperature increases. The temperature dependences on the integration intensities of the transient kinetics are consistent with the temperature dependences on the UCL intensities. The temperature dependence degrees of samples 2–4 are more significant than that of sample 1, which can be simply explained by the thermally activated non-radiative transitions. These substantial temperature effects on the transient and steady-state UCLs could be attributed to Er^{3+}-Er^{3+} ion interactions (corresponding to concentration quenching) of the higher Er^{3+} doping samples in which the energy from one Er^{3+} ion in an excited state is transferred to another excited Er^{3+} ion, as shown in Fig. 6(b) ($^4S_{3/2} + {^4I_{15/2}} \rightarrow {^4I_{13/2}} + {^4I_{9/2}}$, $^2H_{11/2} + {^4F_{7/2}} \rightarrow {^4F_{9/2}} + {^2H_{9/2}}$, $^4S_{3/2} + {^4I_{13/2}} \rightarrow {^4I_{11/2}} + {^4F_{9/2}}$) [19, 55]. The τ_{decay} value and transient intensity decreases of the 542-nm emissions can be attributed to direct quenching of the $^4S_{3/2}$ level and quenching of the $^4F_{7/2}$ level, respectively. The ion interaction quenching could directly or indirectly yield the populations of the 655-nm emitting levels [1, 19]. Such phenomenon should also exist in sample 1, but not to such a significant degree as that in the other three samples.

In samples 2–4, the temperature dependence of the UCL kinetics at 655 nm is similar to that at 542 nm (Figs. S2 and S3 in the ESM). The integration intensity variations of the transient kinetics are significantly different than the UCL intensity variations. The kinetic variations indicate that the concentration quenching also accelerates the transition of the $^4F_{9/2}$ level with the temperature increase, which is similar to the behavior of the 542-nm emission. From the steady-state PL spectra, especially for samples 3 and 4, the 655-nm emission intensities slightly change with increasing temperature, while the 542-nm emission intensities significantly decrease. As mentioned above, this phenomenon indicates that the concentration quenching of the 542-nm emission, at least in part, produces the populations of the 655-nm emitting level [19, 55]. The concentration quenching effect on the $^4F_{9/2}$ level could also explain the one-to-one increase of the 655-nm UCL intensities that result from the concentration quenching of the 542-nm emissions, which could not be observed.

There is another issue worth noting, which is that the transient intensity variations of the 655-nm emission transient kinetics is not consistent with the steady-state PL intensity variations as the temperature increases. This can be attributed to the highly complicated population processes at the 655-nm emitting level, which are strongly associated with the population concentration of the lower levels, such as $^4I_{13/2}$. This is because the UCL process that is excited by a single 974-nm pulsed laser could not fully depict the complicated continuous ETU processes.

3 Conclusions

We clarified the temperature effect on the concentration quenching mechanism by changing the Er^{3+} doping concentration in $NaLuF_4$ nanoparticles. At room temperature, both the steady-state PL spectroscopies and transient UCL kinetics showed significant concentration quenching effects and red dominant luminescence for the UCNPs with higher Er^{3+} doping concentrations. The Er^{3+} PL intensity increased with decreasing temperature, an effect that was much more prominent for the UCNPs with higher Er^{3+} doping concentrations. At cryogenic temperatures (< 160 K), both the PL intensities and the luminescence decay behaviors suggested that the concentration quenching mechanism is switched off. The temperature dependence of the luminescence decay was consistent with that of the state-steady PL intensity, and both exhibited that the concentration quenching could be dominated by temperature. This work highlights the significant temperature effect on the concentration quenching of RE luminescence from UCNPs, and provides an in-depth understanding of the underlying mechanism, which will be beneficial for further development and applications of UCNPs.

4 Experimental

4.1 Chemicals and materials

RE oxides (Yb_2O_3 (99.9%), Lu_2O_3 (99.9%), and Er_2O_3 (99.9%)) were purchased from Beijing Lansu Co. China. RE chlorides ($LuCl_3$, $YbCl_3$, and $ErCl_3$) were obtained by dissolving the metal oxides in 10% hydrochloric solutions and then completely evaporating the water. 1-Octadecene (ODE, 95%), oleic acid (OA, > 95%), NaOH, NH_4F, and nitrosonium tetrafluoroborate ($NOBF_4$) were purchased from Alfa Aesar Ltd. All other chemical reagents were of analytical grade and were used directly without further purification.

4.2 Characterization

The morphology and size of the nanoparticles were determined at 200 kV using low- to high-resolution TEM (JEOL JEM-2010). The prepared samples were dispersed in cyclohexane or ethanol and dropped onto the surface of a copper grid for TEM analysis. Ultraviolet–visible–near infrared absorption spectra were measured using a UV-3600 spectrophotometer (Shimadzu, Japan). Energy-dispersive X-ray analysis of the samples was also performed during the high-resolution TEM measurements. Powder XRD measurements were performed using a Shimadzu 7000 X-ray diffractometer at a scanning rate of $2°\cdot min^{-1}$ in the 2θ range from 10° to 70° (Cu $K\alpha$ radiation, $\lambda = 1.54$ Å). DLS experiments were performed using a Zetasizer Nano ZS90 zeta potential analyzer (Malvern). Steady-state PL spectra were measured using a fluorescence spectrophotometer (FLS980, Edinburgh Instruments), excited by an external CW 980-nm diode laser (Changchun New Industries Optoelectronics Tech Co., MDL-H-980-5W). The time-resolved PL spectra were collected using an FLS980 spectrophotometer combined with a digital oscilloscope (Lecroy, HDO4054) as the kinetic data recorder. The 974-nm pulse generated by a YAG laser (355 nm, 7 ns, 10 MHz) pumped optical parametric oscillator sets was used as the pump source. All the PL studies were recorded at 77–310 K.

4.3 Preparation of the four samples with different Er^{3+} doping concentrations

In a general procedure, $NaLuF_4$ UCNPs with different Er^{3+} doping concentrations (2%, 5%, 10%, and 20%) were prepared using a traditional solvothermal method. Firstly, 7 mL of OA and 15 mL of ODE were each added to four 100-mL three-necked flasks; then, different ratios of RE chlorides ($LuCl_3$:$ErCl_3$:$YbCl_3$ = 78:20:2, 75:20:5, 70:20:10, and 60:20:20) were respectively added to the four flasks following by heated to 160 ℃ under an argon atmosphere to form a transparent solution. After cooling to room temperature, 4 mL of a methanol solution containing NaOH (2.5 mmol) and NH_4F (4 mmol) were then respectively added to these flasks and stirred for 30 min under vacuum. Subsequently, the solutions were heated to 295 ℃ for 1 h under an argon atmosphere to obtain the $NaLuF_4$ UCNPs with different Er^{3+} doping concentrations (2%, 5%, 10%, and 20%). An excessive amount of ethanol was poured into the resultant solutions to separate out the products after naturally cooling to room temperature, and the products were washed with ethanol and cyclohexane three times. The obtained four groups of white UCNPs were dried under vacuum.

Acknowledgements

This work was supported by the National Natural Science Foundation of China (Nos. 21373268, 21301121, and 21227803), the open funding of Renmin University of China (Nos. 15XNLQ04 and 10XNI007), and the open funding of the State Key Laboratory on Integrated Optoelectronics of Jilin University (No. IOSKL2015KF33).

Electronic Supplementary Material: Supplementary material (further details of discussion on the two green emissions of Er^{3+}, the figures of $R_{r/g}$ and decay time dependence on temperature and doping concentration) is available in the online version of this article at https://doi.org/10.1007/s12274-017-1828-4.

References

[1] Auzel, F. Upconversion and anti-stokes processes with f and d ions in solids. *Chem. Rev.* **2004**, *104*, 139–174.

[2] Bloembergen, N. Solid state infrared quantum counters. *Phys. Rev. Lett.* **1959**, *2*, 84–85.

[3] Gamelin, D. R.; Güdel, H. U. Design of luminescent inorganic materials: New photophysical processes studied by optical spectroscopy. *Acc. Chem. Res.* **2000**, *33*, 235–242.

[4] Dong, H.; Sun, L. D.; Yan, C. H. Energy transfer in lanthanide upconversion studies for extended optical applications. *Chem. Soc. Rev.* **2015**, *44*, 1608–1634.

[5] Liu, Y. Y.; Zhang, J. W.; Zuo, C. J.; Zhang, Z.; Ni, D. L.; Zhang, C.; Wang, J.; Zhang, H.; Yao, Z. W.; Bu, W. B. Upconversion nano-photosensitizer targeting into mitochondria for cancer apoptosis induction and cyt c fluorescence monitoring. *Nano Res.* **2016**, *9*, 3257–3266.

[6] Li, X. M.; Zhang, F.; Zhao, D. Y. Lab on upconversion nanoparticles: optical properties and applications engineering via designed nanostructure. *Chem. Soc. Rev.* **2015**, *44*, 1346–1378.

[7] Tan, G. R.; Wang, M. H.; Hsu, C. Y.; Chen, N. G.; Zhang, Y. Small upconverting fluorescent nanoparticles for biosensing and bioimaging. *Adv. Opt. Mater.* **2016**, *4*, 984–997.

[8] Dong, H.; Du, S. R.; Zheng, X. Y.; Lyu, G.-M.; Sun, L. D.; Li, L. D.; Zhang, P. Z.; Zhang, C.; Yan, C. H. Lanthanide nanoparticles: From design toward bioimaging and therapy. *Chem. Rev.* **2015**, *115*, 10725–10815.

[9] Chen, G. Y.; Ågren, H.; Ohulchanskyy, T. Y.; Prasad, P. N. Light upconverting core-shell nanostructures: Nanophotonic control for emerging applications. *Chem. Soc. Rev.* **2015**, *44*, 1680–1713.

[10] Ding, X.; Liu, J. H.; Liu, D. P.; Li, J. Q.; Wang, F.; Li, L. J.; Wang, Y. H.; Song, S. Y.; Zhang, H. J. Multifunctional core/satellite polydopamine@Nd^{3+}-sensitized upconversion nanocomposite: A single 808 nm near-infrared light-triggered theranostic platform for *in vivo* imaging-guided photothermal therapy. *Nano Res.* **2017**, *10*, 3434–3446.

[11] Zhou, B.; Shi, B. Y.; Jin, D. Y.; Liu, X. G. Controlling upconversion nanocrystals for emerging applications. *Nat. Nanotechnol.* **2015**, *10*, 924–936.

[12] Zhou, J.; Liu, Q.; Feng, W.; Sun, Y.; Li, F. Y. Upconversion luminescent materials: Advances and applications. *Chem. Rev.* **2015**, *115*, 395–465.

[13] Zheng, W.; Huang, P.; Tu, D. T.; Ma, E.; Zhu, H. M.; Chen, X. Y. Lanthanide-doped upconversion nano-bioprobes: Electronic structures, optical properties, and biodetection. *Chem. Soc. Rev.* **2015**, *44*, 1379–1415.

[14] Chen, G. Y.; Qiu, H. L.; Prasad, P. N.; Chen, X. Y. Upconversion nanoparticles: Design, nanochemistry, and applications in theranostics. *Chem. Rev.* **2014**, *114*, 5161–5214.

[15] Sun, L. D.; Wang, Y.-F.; Yan, C. H. Paradigms and challenges for bioapplication of rare earth upconversion luminescent nanoparticles: Small size and tunable emission/excitation spectra. *Acc. Chem. Res.* **2014**, *47*, 1001–1009.

[16] Idris, N. M.; Jayakumar, M. K. G.; Bansal, A.; Zhang, Y. Upconversion nanoparticles as versatile light nanotransducers for photoactivation applications. *Chem. Soc. Rev.* **2015**, *44*, 1449–1478.

[17] Yang, D. M.; Ma, P. A.; Hou, Z. Y.; Cheng, Z. Y.; Li, C. X.; Lin, J. Current advances in lanthanide ion (Ln^{3+})-based upconversion nanomaterials for drug delivery. *Chem. Soc. Rev.* **2015**, *44*, 1416–1448.

[18] Dai, Y. L.; Xiao, H. H.; Liu, J. H.; Yuan, Q. H.; Ma, P. A.; Yang, D. M.; Li, C. X.; Cheng, Z. Y.; Hou, Z. Y.; Yang, P. P. et al. *In vivo* multimodality imaging and cancer therapy by near-infrared light-triggered trans-platinum pro-drug-conjugated upconverison nanoparticles. *J. Am. Chem. Soc.* **2013**, *135*, 18920–18929.

[19] Liu, G. K. Advances in the theoretical understanding of photon upconversion in rare-earth activated nanophosphors. *Chem. Soc. Rev.* **2015**, *44*, 1635–1652.

[20] Tu, L. P.; Liu, X. M.; Wu, F.; Zhang, H. Excitation energy migration dynamics in upconversion nanomaterials. *Chem. Soc. Rev.* **2015**, *44*, 1331–1345.

[21] Johnson, N. J. J.; He, S.; Diao, S.; Chan, E. M.; Dai, H. J.; Almutairi, A. Direct evidence for coupled surface and concentration quenching dynamics in lanthanide-doped nanocrystals. *J. Am. Chem. Soc.* **2017**, *139*, 3275–3282.

[22] Wei, W.; Chen, G. Y.; Baev, A.; He, G. S.; Shao, W.; Damasco, J.; Prasad, P. N. Alleviating luminescence concentration quenching in upconversion nanoparticles through organic dye sensitization. *J. Am. Chem. Soc.* **2016**, *138*, 15130–15133.

[23] Wei, W.; Zhang, Y.; Chen, R.; Goggi, J.; Ren, N.; Huang, L.; Bhakoo, K. K.; Sun, H. D.; Tan, T. T. Y. Cross relaxation induced pure red upconversion in activator- and sensitizer-rich lanthanide nanoparticles. *Chem. Mater.* **2014**, *26*, 5183–5186.

[24] Quimby, R. S.; Aitken, B. G. Multiphonon energy gap law in rare-earth doped chalcogenide glass. *J. Non-Cryst. Solids* **2003**, *320*, 100–112.

[25] Zhao, J. B.; Jin, D. Y.; Schartner, E. P.; Lu, Y. Q.; Liu, Y. J.; Zvyagin, A. V.; Zhang, L. X.; Dawes, J. M.; Xi, P.; Piper, J. A. et al. Single-nanocrystal sensitivity achieved by enhanced upconversion luminescence. *Nat. Nanotechnol.* **2013**, *8*, 729–734.

[26] Wang, J.; Deng, R. R.; MacDonald, M. A. B.; Chen, B. L.; Yuan, J. K.; Wang, F.; Chi, D. Z.; Hor, T. A. A.; Zhang, P.; Liu, G. K. et al. Enhancing multiphoton upconversion through energy clustering at sublattice level. *Nat. Mater.* **2014**, *13*, 157–162.

[27] Liu, N.; Qin, W. P.; Qin, G. S.; Jiang, T.; Zhao, D. Highly Plasmon-enhanced upconversion emissions from Au@β-$NaYF_4$:Yb,Tm hybrid nanostructures. *Chem. Commun.* **2011**, *47*, 7671–7673.

[28] Chen, B.; Liu, Y.; Xiao, Y.; Chen, X.; Li, Y.; Li, M. Y.;

Qiao, X. S.; Fan, X. P.; Wang, F. Amplifying excitation-power sensitivity of photon upconversion in a $NaYbF_4$:Ho nanostructure for direct visualization of electromagnetic hotspots. *J. Phys. Chem. Lett.* **2016**, *7*, 4916–4921.

[29] Li, X. Y.; Liu, X. W.; Chevrier, D. M.; Qin, X.; Xie, X. J.; Song, S. Y.; Zhang, H. J.; Zhang, P.; Liu, X. G. Energy migration upconversion in manganese(II)-doped nanoparticles. *Angew. Chem., Int. Ed.* **2015**, *54*, 13312–13317.

[30] Ding, Y. D.; Wu, F.; Zhang, Y. L.; Liu, X. M.; de Jong, E. M. L. D.; Gregorkiewicz, T.; Hong, X.; Liu, Y. C.; Aalders, M. C. G.; Buma, W. J. et al. Interplay between static and dynamic energy transfer in biofunctional upconversion nanoplatforms. *J. Phys. Chem. Lett.* **2015**, *6*, 2518–2523.

[31] Wang, F.; Liu, X. G. Multicolor tuning of lanthanide-doped nanoparticles by single wavelength excitation. *Acc. Chem. Res.* **2014**, *47*, 1378–1385.

[32] Bünzli, J. C. G. Benefiting from the unique properties of lanthanide ions. *Acc. Chem. Res.* **2006**, *39*, 53–61.

[33] Chen, Z. G.; Chen, H. L.; Hu, H.; Yu, M. X.; Li, F. Y.; Zhang, Q.; Zhou, Z. G.; Yi, T.; Huang, C. H. Versatile synthesis strategy for carboxylic acid-functionalized upconverting nanophosphors as biological labels. *J. Am. Chem. Soc.* **2008**, *130*, 3023–3029.

[34] Zhang, F.; Wan, Y.; Yu, T.; Zhang, F. Q.; Shi, Y. F.; Xie, S. H.; Li, Y. G.; Xu, L.; Tu, B.; Zhao, D. Y. Uniform nanostructured arrays of sodium rare-earth fluorides for highly efficient multicolor upconversion luminescence. *Angew. Chem., Int. Ed.* **2007**, *46*, 7976–7979.

[35] Li, Z. Q.; Zhang, Y. An efficient and user-friendly method for the synthesis of hexagonal-phase $NaYF_4$:Yb, Er/Tm nanocrystals with controllable shape and upconversion fluorescence. *Nanotechnology* **2008**, *19*, 345606.

[36] Wang, G. F.; Peng, Q.; Li, Y. D. Lanthanide-doped nanocrystals: Synthesis, optical-magnetic properties, and applications. *Acc. Chem. Res.* **2011**, *44*, 322–332.

[37] Zhou, J.; Liu, Z.; Li, F. Y. Upconversion nanophosphors for small-animal imaging. *Chem. Soc. Rev.* **2012**, *41*, 1323–1349.

[38] Zhang, Y. L.; Liu, X. H.; Lang, Y. B.; Yuan, Z.; Zhao, D.; Qin, G. S.; Qin, W. P. Synthesis of ultra-small $BaLuF_5:Yb^{3+},Er^{3+}$@$BaLuF_5:Yb^{3+}$ active-core-active-shell nanoparticles with enhanced up-conversion and down-conversion luminescence by a layer-by-layer strategy. *J. Mater. Chem. C* **2015**, *3*, 2045–2053.

[39] Heer, S.; Kömpe, K.; Güdel, H. U.; Haase, M. Highly efficient multicolour upconversion emission in transparent colloids of lanthanide-doped $NaYF_4$ nanocrystals. *Adv. Mater.* **2004**, *16*, 2102–2105.

[40] Krämer, K. W.; Biner, D.; Frei. G.; Güdel, H. U.; Hehlen, M. P.; Lüthi, S. R. Hexagonal sodium yttrium fluoride based green and blue emitting upconversion phosphors. *Chem. Mater.* **2004**, *16*, 1244–1251.

[41] Yi, G. S.; Chow, G. M. Synthesis of hexagonal-phase $NaYF_4$:Yb, Er and $NaYF_4$:Yb, Tm nanocrystals with efficient up-conversion fluorescence. *Adv. Funct. Mater.* **2006**, *16*, 2324–2329.

[42] Ding, M. Y.; Chen, D. Q.; Yin, S. L.; Ji, Z. G.; Zhong, J. S.; Ni, Y.; Lu, C. H.; Xu, Z. Z. Simultaneous morphology manipulation and upconversion luminescence enhancement of β-$NaYF_4:Yb^{3+}/Er^{3+}$ microcrystals by simply tuning the KF dosage. *Sci. Rep.* **2015**, *5*, 12745.

[43] Liu, Q.; Sun, Y.; Yang, T. S.; Feng, W.; Li, C. G.; Li, F. Y. Sub-10 nm hexagonal lanthanide-doped $NaLuF_4$ upconversion nanocrystals for sensitive bioimaging *in vivo*. *J. Am. Chem. Soc.* **2011**, *133*, 17122–17125.

[44] Li, C. X.; Quan, Z. W.; Yang, P. P.; Huang, S. S.; Lian, H. Z.; Lin, J. Shape-controllable synthesis and upconversion properties of lutetium fluoride (doped with Yb^{3+}/Er^{3+}) microcrystals by hydrothermal process. *J. Phys. Chem. C* **2008**, *112*, 13395–13404.

[45] Shi, F.; Wang, J. S.; Zhai, X. S.; Zhao, D.; Qin, W. P. Facile synthesis of β-$NaLuF_4$: Yb/Tm hexagonal nanoplates with intense ultraviolet upconversion luminescence. *CrystEngComm* **2011**, *13*, 3782–3787.

[46] Xiang, G. T.; Zhang, J. H.; Hao, Z. D.; Zhang, X.; Pan, G.-H.; Luo, Y. S.; Zhao, H. F. Decrease in particle size and enhancement of upconversion emission through Y^{3+} ions doping in hexagonal $NaLuF_4:Yb^{3+}/Er^{3+}$ nanocrystals. *CrystEngComm* **2015**, *17*, 3103–3109.

[47] Zheng, K. Z.; He, G. H.; Song, W. Y.; Bi, X. Q.; Qin, W. P. A strategy for enhancing the sensitivity of optical thermometers in β-$NaLuF_4:Yb^{3+}/Er^{3+}$ nanocrystals. *J. Mater. Chem. C* **2015**, *3*, 11589–11594.

[48] Zeng, J. H.; Su, J.; Li, Z. H.; Yan, R. X.; Li, Y. D. Synthesis and upconversion luminescence of hexagonal-phase $NaYF_4$:Yb, Er^{3+} phosphors of controlled size and morphology. *Adv. Mater.* **2005**, *17*, 2119–2123.

[49] Berry, M. T.; May, P. S. Disputed mechanism for NIR-to-red upconversion luminescence in $NaYF_4:Yb^{3+},Er^{3+}$. *J. Phys. Chem. A* **2015**, *119*, 9805–9811.

[50] Lei, P. P.; Zhang, P.; Yuan, Q. H.; Wang, Z.; Dong, L. L.; Song, S. Y.; Xu, X.; Liu, X. L.; Feng, J.; Zhang, H. J. Yb^{3+}/Er^{3+}-codoped Bi_2O_3 nanospheres: probe for upconversion luminescence imaging and binary contrast agent for computed tomography imaging. *ACS Appl. Mater. Interfaces* **2015**, *7*, 26346–26354.

[51] Liu, Y. S.; Tu, D. T.; Zhu, H. M.; Chen, X. Y. Lanthanide-

doped luminescent nanoprobes: Controlled synthesis, optical spectroscopy, and bioapplications. *Chem. Soc. Rev.* **2013**, *42*, 6924–6958.

[52] Xu, X.; Zhang, P.; Yuan, Q. H.; Lei, P. P.; Dong, L. L.; Wang, Z.; Liu, X. L.; Song, S. Y.; Feng, J.; Zhang, H. J. Dual-functional α-NaYb(Mn)F_4:Er^{3+}@$NaLuF_4$ nanocrystals with highly enhanced red upconversion luminescence. *RSC Adv.* **2016**, *6*, 33493–33500.

[53] Wang, Y.; Tu, L. P.; Zhao, J. W.; Sun, Y. J.; Kong, X. G.; Zhang, H. Upconversion luminescence of β-$NaYF_4$: Yb^{3+}, Er^{3+}@β-$NaYF_4$ core/shell nanoparticles: Excitation power, density and surface dependence. *J. Phys. Chem. C* **2009**, *113*, 7164–7169.

[54] Li, X. M.; Wang, R.; Zhang, F.; Zhao, D. Y. Engineering homogeneous doping in single nanoparticle to enhance upconversion efficiency. *Nano Lett.* **2014**, *14*, 3634–3639.

[55] Anderson, R. B.; Smith, S. J.; May, P. S.; Berry, M. T. Revisiting the NIR-to-visible upconversion mechanism in β-$NaYF_4$:Yb^{3+},Er^{3+}. *J. Phys. Chem. Lett.* **2014**, *5*, 36–42.